

Laser-assisted copper oxidation to enhance electrochemical performances of lithium-metal anode-less batteries

*Original*

Laser-assisted copper oxidation to enhance electrochemical performances of lithium-metal anode-less batteries / Tallone, Paolo; Spriano, Silvia; Versaci, Daniele; Tori, Alice; Bodoardo, Silvia. - In: JOURNAL OF ENERGY STORAGE. - ISSN 2352-152X. - 149:(2026), pp. 1-12. [10.1016/j.est.2026.120337]

*Availability:*

This version is available at: 11583/3006468 since: 2026-01-12T15:00:09Z

*Publisher:*

Elsevier

*Published*

DOI:10.1016/j.est.2026.120337

*Terms of use:*

This article is made available under terms and conditions as specified in the corresponding bibliographic description in the repository

*Publisher copyright*

(Article begins on next page)



## Research papers

# Laser-assisted copper oxidation to enhance electrochemical performances of lithium-metal anode-less batteries

Paolo Tallone<sup>a,\*</sup>, Silvia Spriano<sup>a</sup>, Daniele Versaci<sup>a</sup>, Alice Tori<sup>b</sup>, Silvia Bodoardo<sup>a</sup>

<sup>a</sup> Politecnico di Torino, Department of Applied Science and Technology, Electrochemistry Group, Corso Duca degli Abruzzi, 24, 10129, Turin, Italy

<sup>b</sup> Osai Automation Systems SpA, Via della Cartiera 4, 10010, Parella (TO), Italy

## ARTICLE INFO

## Keywords:

Laser processing  
Current collector  
Anode-less  
Li-metal battery

## ABSTRACT

Anode-less lithium metal batteries (ALLMBs) have been considered promising candidates for future energy storage applications because of their high energy density and simplified manufacturing. However, issues in lithium dendrite formation and capacity degradation prevent their practical application. This study introduces a novel, reagent-free approach for enhancing ALLMBs performance through laser-induced copper oxidation under ambient conditions to create precisely controlled  $\text{CuO}_x$  surface layers on the copper current collector (CC). The oxidized surface converts to  $\text{Li}_2\text{O}$  in the first charge, forming a stable artificial solid electrolyte interphase (SEI), that enables uniform lithium deposition with reduced nucleation overpotential.

Electrochemical tests show  $\text{Cu\_LS1000}$  optimally balances conductivity and oxide for better Coulombic efficiency (CE) and cycling stability. Specifically, the  $\text{Cu\_LS1000}$  exhibited higher CE in half-cells and higher capacity retention compared to unprocessed copper. Full-cell testing with lithium iron phosphate (LFP) cathodes validated improved rate capability at low to moderate current densities. Excessive oxidation ( $\text{Cu\_LS300}$ ) compromised cycling stability due to higher polarization and lithium consumption during initial activation. This work proves that laser-assisted copper oxidation is a scalable and environmentally friendly technique to address the critical limitations of ALLMBs. The approach underlines the potential of laser-engineered CCs, enabling safer and more efficient anode-less battery technologies.

## 1. Introduction

The growing demand for high-performance energy storage systems in applications such as electric vehicles (EVs), portable electronics, and renewable energy integration has driven intense research into next-generation battery technologies. Among these, lithium metal batteries (LMBs) have emerged as one of the most interesting and promising candidates due to their incomparable energy density and lightweight. Lithium metal anodes offer an exceptionally high theoretical specific capacity ( $3860 \text{ mAh g}^{-1}$ ) and a very low redox potential ( $-3.04 \text{ V}$  vs. the standard hydrogen electrode), potentially surpassing the capacity of conventional lithium-ion batteries based on graphite anodes [1–3]. Among them, anode-less lithium metal batteries (ALLMBs) are particularly promising owing to their high energy density and simple fabrication procedure [4–6]. Indeed, in an anode-less battery, there is only a current collector as the anode without Li metal in the initial assembly of the cell, which means that this approach significantly reduces both the volume and mass of the anode. More in detail,  $\text{Li}^+$  ions are extracted

from the cathode material, which is the sole source of  $\text{Li}^+$  ions in this configuration during charging in an ALLMB, and then electrodeposited as Li metal on the current collector, at the anode side. During discharge, the  $\text{Li}^+$  ions are stripped from the anode and intercalate back into the cathode material [7,8]. In this work, we define ‘anode-less’ as a zero-excess lithium configuration where the initial cell assembly contains no metallic lithium on the negative electrode. The copper current collector serves as the substrate for plating, and the cathode material acts as the sole source of active lithium inventory.

Actually, the development of high-performance ALLMBs faces two critical challenges in practical applications: safety and efficiency. One of the most critical issues arises from the tendency of the lithium metal to deposit unevenly during the repeated charging and discharging cycles due to the formation of dendrites. These needle-like structures could pierce the separator and possibly cause internal short circuits, which could result in a significant risk of fires and other safety hazards [9]. In addition to dendrite formation, the continued accumulation of inactive ‘dead’ lithium and electrolyte decomposition during cycling further

\* Corresponding author.

E-mail address: [paolo.tallone@polito.it](mailto:paolo.tallone@polito.it) (P. Tallone).

<https://doi.org/10.1016/j.est.2026.120337>

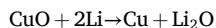
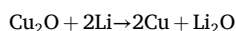
Received 12 August 2025; Received in revised form 10 December 2025; Accepted 1 January 2026

Available online 10 January 2026

2352-152X/© 2026 The Authors. Published by Elsevier Ltd. This is an open access article under the CC BY-NC-ND license (<http://creativecommons.org/licenses/by-nc-nd/4.0/>).

drives performance degradation since these mechanisms result in a linear loss of capacity [10]. These issues necessitate an optimal deposition environment for lithium, specifically at the current collector (CC)-electrolyte interface. If managed properly, this interface can form a stable solid electrolyte interphase (SEI) layer, which is crucial in reducing capacity loss by preventing further decomposition of the electrolytes. A stable SEI layer also supports smooth, dendrite-free lithium plating, which contributes to both the safety and longevity of the battery system [11,12]. Besides electrolyte modifications, which have been intensively studied to stabilize lithium deposition [13–16], another important strategy is optimizing the physical and chemical properties of the current collector. By optimizing these properties, a more favorable environment at the electrode/electrolyte interface may be created, further enhancing lithium deposition and overall cycling stability of ALLMBs [17–19].

Copper is the most commonly used material for current collectors of negative electrodes, but its lithiophobic nature leads to high nucleation potential, which makes uniform lithium deposition difficult. To solve this, many strategies have been investigated, such as fabricating a 3D surface structure to lower the local current density and accommodate the repeated volume changes [20,21] or introducing lithiophilic materials as nucleation sites to lower the lithium nucleation barrier and promote even deposition [22]. Examples include lithiophilic seeds such as metallic fluorides [23], oxides (e.g., ZnO, TiO<sub>2</sub>) [24,25], selenides [26], nitrides (e.g. Cu<sub>3</sub>N) [27], noble metals (e.g. Au, Ag) [20,28], metal-organic frameworks [29], metallic alloys [30] and functionalized materials like N-doped graphene [24]. Among these, copper oxides are promising candidates thanks to their low production cost by simple oxidation of the current collector surface. Their ability to increase the surface lithiophilicity is ascribed to the conversion reaction that happens during the first charging cycle, that leads to the formation of metallic Cu and Li<sub>2</sub>O from Cu<sub>2</sub>O and CuO, following the reactions:



Li<sub>2</sub>O exhibits a significantly smaller lattice mismatch with Li. Therefore, a smaller energy barrier is required to form the Li<sub>2</sub>O–Li interface, making it more likely to result in a uniformly covered lithium metal film [32]. Copper oxide layers have been previously explored using various methods, including thermal treatments [17,33,34], chemical etching [35] and plasma treatments [36,37]. In recent years, laser-based techniques have emerged as a promising approach for modifying the physical and chemical properties of metallic foil surfaces, offering notable economic and environmental advantages [38–42]. Despite this growing interest, to the best of the authors' knowledge, no studies have yet reported the use of laser-based oxidation techniques specifically applied to Cu current collectors for anode-less Li metal batteries.

Here, we report a quick, inexpensive, and reagent-less approach to obtain accurate and controlled oxidation of the Cu foil surface under ambient conditions, which neither requires heating nor chemical agents. The method realizes a homogeneous layer of copper oxide (CuO<sub>x</sub>), which plays a crucial role in the first charge cycle. The CuO<sub>x</sub> layer electrochemically converts into Li<sub>2</sub>O, forming a stable artificial SEI that lowers lithium nucleation overpotential, enhancing lithium metal anode performance. Full cells with LFP cathodes showed significantly improved cycling stability and electrochemical performance using this Cu surface treatment. This simple, scalable process holds promise for advancing next-generation energy storage systems.

## 2. Material and methods

### 2.1. Laser oxidation of the copper current collector

Laser texturing was performed using a Nd:YAG 1064 nm laser

(HyperRapid NX model, Coherent, Germany) with a pulse duration <15 ps. Beam movement and focusing were achieved with a galvanometric scanning head equipped with a 160 mm focal length f-theta lens. A parallel line scanning strategy and different scanning speeds (from 300 to 1000 mm/s) were utilized to achieve the desired degree of oxidation at a selected power of 10 W at a repetition rate of 50 kHz to obtain laser-modified samples. All the experiments were performed in the air. Table 1 summarizes the laser parameters used to obtain the samples.

### 2.2. Characterization of laser-textured current collectors

The surface morphology was observed by means of Scanning Electron Microscopy (SUPRA ZEISS FE-SEM) coupled with Energy-dispersive X-ray spectroscopy (EDS).

Diffuse reflectance (DR) UV–Vis–NIR characterization was performed on the samples.

The spectra were run on a (Uv–Vis, Shimadzu, UV 2600) spectrophotometer, working in the range of 200–900 nm. The DR UV–Vis spectra were recorded in air, at room temperature and reported in the Kubelka-Munk function (F) as shown in eq. (1):

$$F(R_\infty) = \frac{(1 - R_\infty)^2}{2R_\infty} = \frac{K}{s}$$

where  $R_\infty$  is the reflectance of a hypothetical infinitely thick layer of the sample.  $K$  is the molar absorption coefficient and  $s$  is the scattering coefficient.

The crystallographic properties of the samples were examined through grazing incidence X-ray diffraction (GI-XRD) with a Panalytical X'pert Pro (Cu K $\alpha$  radiation, the wavelength of 1.5406 Å). Raman spectra were recorded using a Senterra spectrometer from Bruker Optics with OPUS 7.5 software, employing a 532 nm excitation laser.

### 2.3. Cathode preparation and electrochemical characterization

Cathode electrodes were fabricated using the solvent casting method. A water-based cathodic slurry was created by combining Lithium Iron Phosphate (LFP, MTI Corporation), Carbon Black C-ENERGY C45 (Imerys Graphite & Carbon Corporation), and Sodium Carboxymethylcellulose (Na-CMC, DAICEL) in a weight ratio of 85:10:5, respectively. To prepare the slurry, Na-CMC was dissolved in deionized water to form a 5 wt% solution. Once the binder was fully dissolved, the active material and carbon black were added, and the mixture was ball-milled for 20 min at 15 Hz. The resulting slurry was then cast onto aluminum current collectors (battery grade, MTI Corporation) using the Doctor Blade technique with an automatic film applicator (Sheen 1133 N, speed of 10 mm/s). After the solvent evaporated in the air at 50 °C for 1 h, 1.766 cm<sup>2</sup> disks were punched out using a Compact Precision Disc Cutter MSK-T-07 and vacuum dried at 120 °C for 4 h in a Büchi Glass Oven B-585, before cell assembly. The active material mass loadings were between 6.4 and 6.6 mg/cm<sup>2</sup>. Cell assembly was performed in an argon-filled glove box (MBraun Labstar, H<sub>2</sub>O and O<sub>2</sub> content <1 ppm) with a two-electrode 2032 coin cell configuration. A polymer membrane (Celgard 2325) served as the separator and was soaked with 100  $\mu$ L of electrolyte solution of 1 M LiTFSI in a 1:1 volume ratio of dioxolane

**Table 1**

Laser process parameters used to obtain the different laser-modified current collectors.

Sample name	Scanning speed mm/s	Laser power W	Repetition rate kHz
Cu_LS300	300	10	50
Cu_LS500	500	10	50
Cu_LS750	750	10	50
Cu_LS1000	1000	10	50
Cu_LS1000-75	1000	7.5	50
Cu_LS1000-50	1000	5	50

(DOL) and dimethoxyethane (DME) (Solvionic), along with 0.25 M  $\text{LiNO}_3$  as an additive. For all the electrochemical tests performed in this work, the separator, electrolyte, and electrolyte amount were kept consistent. The electrolyte-to-capacity ratio was approximately  $60 \mu\text{L mA h}^{-1}$  for full cell tests. The LFP cathodes were tested electrochemically using pristine Cu, Cu\_LS1000, and Cu\_LS300 as counter electrodes in an anode-less full-cell configuration. The cells are strictly cathode-limited. The LFP cathode provides the only available lithium, corresponding to a theoretical N/P ratio of 0 regarding metallic lithium. No pre-lithiation steps were used. For full cells, formation consisted of three initial cycles at 0.1C to stabilize the interface before rate capability. All electrochemical tests were conducted at room temperature. Coin cells were tested without external stack pressure. The cycling performance of the cells was evaluated through galvanostatic discharge-charge cycling (GC) on an Arbin LBT-21084 under various current regimes within the voltage range of 3 to 4.2 V ( $1\text{C} = 175 \text{ mA g}^{-1}$ ). Cyclic Voltammetry (CV) was performed using a versatile multichannel potentiostat (VMP-3 Biologic) at a scan rate of 0.05 mV/s. Half-cells were prepared using the same two-electrodes setup, using pure metallic Li as a counter electrode. Before the actual plating, cells were activated by three discharge-charge cycles between 0.01 and 1 V at  $0.05 \text{ mA cm}^{-2}$ . Electrodes for symmetrical cells were prepared depositing  $2 \text{ mA h cm}^{-2}$  or  $4 \text{ mA h cm}^{-2}$  of Li on the copper samples. Two identical anodes were used to assemble the cells. The measurements were performed at  $1 \text{ mA cm}^{-2}$  with the capacity of  $1 \text{ mA h cm}^{-2}$ . The cycling performance of three-electrode cells was assessed using a PATCell (EL Cell) and a versatile multichannel potentiostat (VMP-3 Biologic), with a lithium ring as the reference electrode. This three-electrode setup enabled control and separation of the voltage profiles for both the anode and cathode throughout the

charge and discharge cycles.

### 3. Results and discussion

#### 3.1. Chemical and physical characterization

The surface morphology and composition of the laser-processed and pristine copper samples were observed by means of SEM coupled with EDS analysis. Table S1 and Fig. S1 in the Supporting Information report the EDS and DR-UV-Vis results for the modified samples with different laser scanning speeds and different laser powers that were initially investigated. As can be seen, only a slight increase in oxygen amount is observed when the laser scanning speed decreased from 750, 500 to 300 mm/s. The same effect can be achieved by increasing the laser power. Therefore, two scanning speeds leading to significant differences in the surface chemical composition—1000 mm/s and 300 mm/s—were selected to produce Cu\_LS1000 and Cu\_LS300, respectively. As can be observed in Fig. 1a–b, the pure Cu sample exhibits a smooth surface, whereas the Cu\_LS1000 (Fig. 1c–d) and Cu\_LS300 (Fig. 1e–f) samples exhibit an increasing quantity of spherical particles of oxide on the surface. Higher magnification images indicate that these bigger particles are actually composed of smaller, agglomerated particles (Fig. 1d, f).

Compositional information was obtained through Energy Dispersive Spectroscopy (EDS). Table 2 summarizes the results of the analysis performed on all three samples. The gradual increase in oxygen content observed from pure Cu to the Cu\_LS300 sample indicates that reducing the laser beam scanning speed over the copper surface enhances the sample overall oxidation. This effect results from a greater overlap between successive laser pulses, leading to a higher fluence deposited on

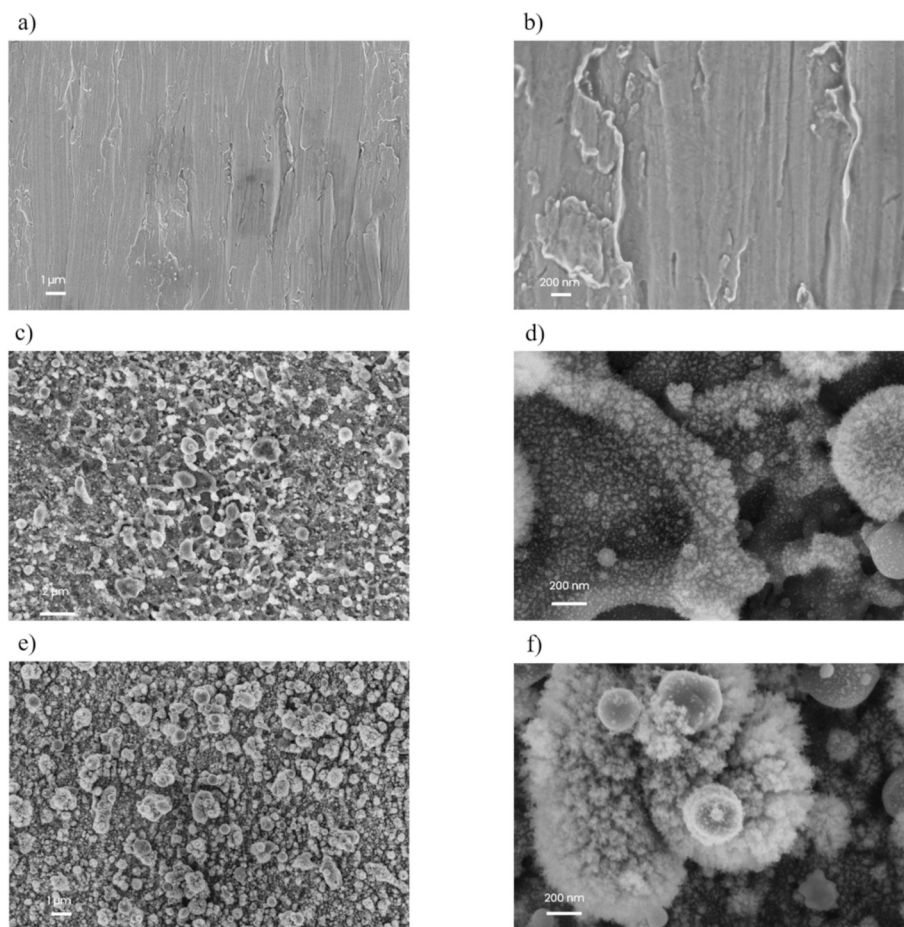


**Fig. 1.** SEM micrographs of the Cu CC at magnifications of a) 5 kX and b) 50 kX, Cu\_LS1000 at a magnification of c) 5kX and d) 50 kX, Cu\_LS300 at magnifications of e) 5 kX and f) 50 kX.

**Table 2**  
Results of EDS analyses performed on pure Cu and laser oxidized copper foils.

Element	Cu %	Cu_LS1000 %	Cu_LS300 %
Copper	98.36	89.58	80.38
Oxygen	1.64	10.42	19.62

the surface. Finely tuning the laser process parameters can therefore allow for precise control of the surface chemistry of the sample.

Diffuse Reflectance UV–Vis (DR-UV-Vis) spectroscopy was employed to investigate the surface oxidation states of the Cu samples following laser processing. The results, shown in Fig. 2a, reveal distinct differences in the absorption characteristics of the samples. For the unprocessed, pure Cu foil, no significant absorption bands were detected across the range of 200–900 nm, indicating minimal or no oxidation.

In contrast, the Cu\_LS1000 and Cu\_LS300 samples exhibited a prominent absorption edge around 550–600 nm. This feature can be attributed to the semiconducting properties of Cu<sub>2</sub>O, which has a reported bandgap of approximately 2.3 eV, corresponding to the observed spectral range. The presence of this absorption edge suggests the formation of Cu<sub>2</sub>O on the surface of these laser-processed samples, indicating partial oxidation to the Cu(I) state.

Additionally, a less intense but notable absorption is observed between 700 and 900 nm, particularly pronounced in the Cu\_LS300 sample. This band is associated with the formation of CuO, a Cu(II) oxide, which absorbs in this region due to its narrower bandgap. The greater intensity of this band in Cu\_LS300 suggests that this sample underwent further oxidation, resulting in a higher quantity of CuO on its surface. This additional CuO formed through the progressive oxidation of Cu<sub>2</sub>O, where Cu(I) was oxidized to Cu(II) under the conditions induced by laser

processing.

Overall, these results indicate that Cu\_LS300 had a higher degree of oxidation compared to Cu\_LS1000, with a more substantial formation of CuO. This demonstrates that careful tuning of laser processing parameters enables control over the oxidation states of the copper atoms, allowing precise tailoring of surface composition to achieve desired properties.

The possibility of carefully controlling the surface chemistry by the laser process is further supported by the Raman analysis results, reported in Fig. 2b, which show no detectable peaks in the 200–1000 cm<sup>-1</sup> range for the pure Cu sample, indicating the absence of Cu oxides. In contrast, the laser-processed samples, Cu\_LS1000 and Cu\_LS300, exhibited distinct Raman peaks, with four prominent bands appearing at 210 cm<sup>-1</sup>, 410 cm<sup>-1</sup>, 530 cm<sup>-1</sup>, and 630 cm<sup>-1</sup>, which correspond to Cu<sub>2</sub>O vibrational modes [43,44].

Additionally, a peak at 290 cm<sup>-1</sup> is evident, whose intensity increases from the Cu\_LS1000 to the Cu\_LS300 sample. This band is attributed to the A<sub>1g</sub> vibrational mode of CuO, suggesting an increased presence of cupric oxide (CuO) at lower laser scanning speeds. This trend further supports the formation of a Cu<sub>2</sub>O/CuO mixture on the laser-processed surfaces, with the ratio of Cu(II) to Cu(I) species increasing as the scanning speed decreases.

Furthermore, the high intensity of the 630 cm<sup>-1</sup> band may also result from the overlap of B<sub>g</sub> symmetry modes from both CuO and Cu<sub>2</sub>O, as these modes fall within the same spectral range. Altogether, these findings indicate that the Cu(II)/Cu(I) ratio can be modified and controlled effectively by adjusting the laser scanning speed during processing.

Raman spectroscopy thus confirms that the laser oxidation process produces a mixed Cu<sub>2</sub>O–CuO layer whose relative phase content depends sensitively on the scanning speed. To quantify this effect, we

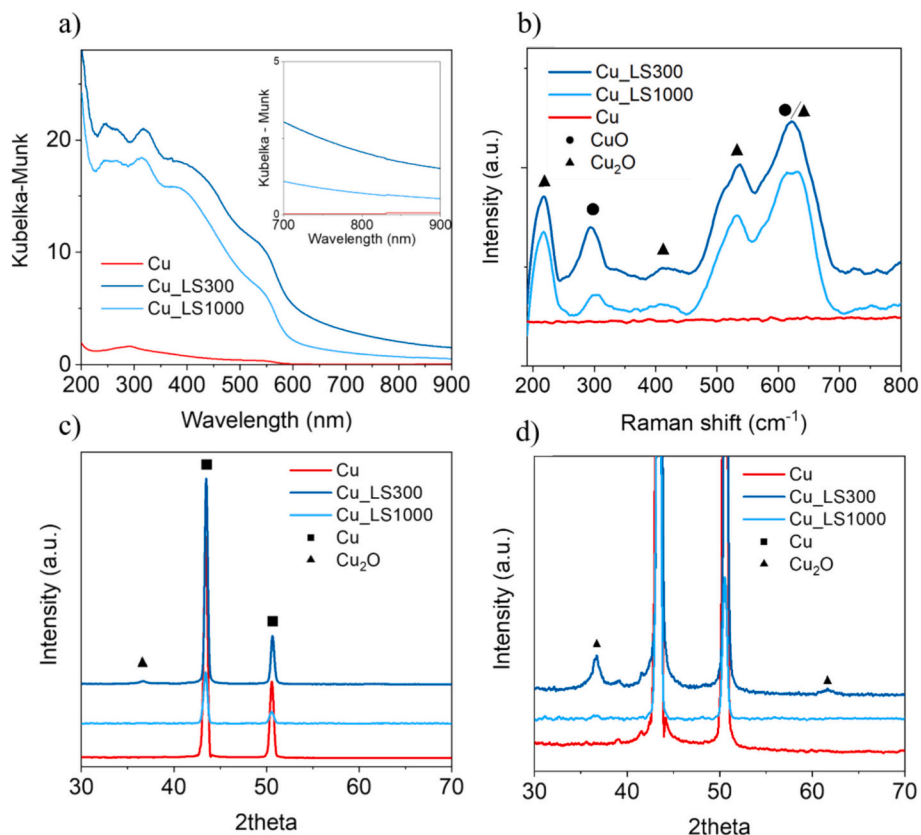


**Fig. 2.** a) DR-UV-Vis spectra of the Cu, Cu\_LS1000 and Cu\_LS300 in the 200–900 nm range. b) Raman spectra of the Cu, Cu\_LS1000 and Cu\_LS300 samples in the range 200–1000 cm<sup>-1</sup>. c) XRD pattern of the Cu, Cu\_LS1000 and Cu\_LS300 samples. d) Zoom in the range 30°–70° and change in the Cu<sub>2</sub>O diffraction peaks for the three samples.

extracted the area ratio  $A_{\text{CuO}}/A_{\text{Cu}_2\text{O}}$  from the  $290\text{ cm}^{-1}$  and  $215\text{ cm}^{-1}$  Raman bands, respectively, obtaining values of 0.27 for Cu\_LS1000 and 0.58 for Cu\_LS300. This semi-quantitative Cu(II)/Cu(I) indicator demonstrates that lower scanning speeds generate a more CuO-rich surface. Since the Cu oxidation state determines the amount of  $\text{Li}_2\text{O}$  formed during the initial conversion reaction, these compositional differences are expected to play a decisive role in the subsequent electrochemical behaviour. A more comprehensive discussion of how this tunable Cu(II)/Cu(I) ratio impacts the electrochemical properties of the electrodes is presented in Section 3.2.

The crystalline structures of the pristine copper and laser-oxidized samples, analyzed by grazing incidence X-ray diffraction (GI-XRD), are shown in Fig. 2c–d. The diffraction patterns for the pristine copper display prominent peaks at  $2\theta$  angles of  $43.31^\circ$ ,  $50.61^\circ$ , and  $74.31^\circ$ , which correspond to reflections from the (111), (200), and (220) planes of face-centered cubic (fcc) Cu.

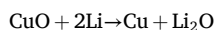
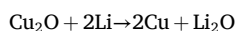
In the laser-treated Cu\_LS300 sample, additional diffraction peaks appear at  $2\theta = 36.51^\circ$  and  $2\theta = 61.5^\circ$ , which are assigned to the (111) and (311) planes of  $\text{Cu}_2\text{O}$  (JCPDS-00-005-0667), indicating the formation of cuprous oxide on the surface during laser processing. The presence of these  $\text{Cu}_2\text{O}$  peaks confirmed the oxidation effect induced by the laser treatment, as the copper surface underwent a partial conversion to cuprous oxide.

Interestingly, no diffraction peaks corresponding to CuO, expected at  $2\theta$  values of  $35.5^\circ$  and  $38.8^\circ$  for the most intense peaks (JCPDS-01-089-5899), are observed in the GI-XRD patterns of the laser-treated samples [45]. This suggests that the CuO likely formed in an amorphous phase that lacked long-range crystallinity and, therefore, did not produce distinct diffraction peaks. This amorphous CuO phase might have formed during the oxidation of the already crystalline  $\text{Cu}_2\text{O}$  layer, as the laser oxidation process was still ongoing.

In conclusion, the phase composition of the laser-induced oxide layer was determined to be a mixture of crystalline  $\text{Cu}_2\text{O}$  and amorphous cupric oxide CuO through a complementary analysis of GI-XRD, Raman, and DR-UV-Vis spectroscopy. The presence of crystalline  $\text{Cu}_2\text{O}$  is unambiguously supported by the observation of distinct diffraction peaks at  $2\theta = 36.51^\circ$  and  $61.5^\circ$  corresponding to the (111) and (311) planes, corroborated by characteristic Raman bands at 210, 410, 530, and  $630\text{ cm}^{-1}$  and a semiconducting absorption edge at 550–600 nm consistent with the 2.3 eV bandgap of  $\text{Cu}_2\text{O}$ . In contrast, CuO was identified solely through spectroscopic signatures sensitive to local atomic bonding and electronic structure, specifically the appearance of the  $A_{1g}$  vibrational mode at  $290\text{ cm}^{-1}$  in the Raman spectra and a broad absorption tail between 700 and 900 nm in the UV-Vis spectra. The complete absence of CuO diffraction peaks (expected at  $35.5^\circ$  and  $38.8^\circ$ ) in the GI-XRD patterns indicates that this secondary phase exists in an amorphous or highly disordered state, lacking long-range crystallinity, likely formed through the further oxidation of the crystalline  $\text{Cu}_2\text{O}$ .

### 3.2. Electrochemical characterization

The bare Cu, Cu\_LS1000 and Cu\_LS300 samples were tested in half-cell configuration with a metallic lithium counter electrode to assess the plating/stripping cycling stability and CE. Before the actual plating, cells were activated by three discharge-charge cycles between 0.01 and 1 V at  $0.05\text{ mA cm}^{-2}$ . During the activation process (Fig. 4a), CuO and  $\text{Cu}_2\text{O}$  present on the electrode surface underwent an electrochemical reaction with lithium, resulting in the transformation into copper and lithium oxide, as represented by the following reactions:



The morphology of the  $\text{Li}_2\text{O}$  layer formed on the Cu\_LS1000 and Cu\_LS300 samples was observed by SEM after the activation (Fig. S2). Microstructures smaller than  $1\text{ }\mu\text{m}$  were observed for both samples.

Although no evident differences in morphology were observed between the two samples, the overall  $\text{Li}_2\text{O}$  amount on the surface was higher for the Cu\_LS300, as evident from the activation voltage curves.

Notably, the  $\text{Li}_2\text{O}$  layer can enhance the lithiophilicity of the substrate surface, reducing the overpotential for subsequent Li plating and thereby improving the cell Coulombic Efficiency, as the uniformity of the Li plating during the first charge, which is important for the long-term stability of the cell [33,34,46].

The plated Li morphology was observed by SEM, after the deposition of  $4\text{ mAh cm}^{-2}$  of metallic Li at  $0.5\text{ mA cm}^{-2}$  current density. The results are reported in Fig. 3a–c. The pure Cu sample (Fig. 3a) exhibited a less compact and homogeneous morphology, with some evident voids and porosities that can facilitate Li dendrites growing during cycling.

SEM micrographs of plated lithium on Cu\_LS1000 (Fig. 3b) and Cu\_LS300 (Fig. 3c) reveal a more compact structure compared to pristine Cu (Fig. 3a), suggesting improved initial Li affinity due to surface oxidation. However, this advantage is counterbalanced by increased internal resistance, which results in faster capacity fade during long-term cycling. Notably, although both oxidized samples (Cu\_LS300 and Cu\_LS1000) promote uniform Li nucleation, only Cu\_LS1000 achieves a favorable balance between morphology, conductivity, and irreversible Li loss.

This is further confirmed by observing Fig. 4b, where the voltage profiles obtained during the Li plating are reported. The Li nucleation overpotential, calculated as the difference between the lowest voltage and the stable voltage plateau, was 34 mV, 20 mV, and 21 mV, respectively for the Cu sample, Cu\_LS1000 and Cu\_LS300, confirming the beneficial properties of the  $\text{Li}_2\text{O}$ -rich surface. However, the poor electrical conductivity of the oxide layer induce a higher polarization, as can be seen by the lower value of the stable voltage plateau reached for the Cu\_LS300 sample ( $-79\text{ mV}$ ) compared to the pure Cu sample ( $-40\text{ mV}$ ). However, Cu\_LS1000 sample exhibited the best compromise between these two effects, with a reduced Li plating overpotential coupled with a cell polarization comparable to the bare Cu sample. Fig. 4e reports the results of the half-cell cycling tests performed on Cu, Cu\_LS1000 and Cu\_LS300 samples. As can be seen, the Cu sample maintained stable cycling performance for approximately 50 cycles, after which its CE declined sharply, falling to 60 % by the 60th cycle. A comparable decline beginning was also seen in Cu\_LS300, around the 80th cycle. In contrast, Cu\_LS1000 showed a more stable cycling behaviour, maintaining values over 90 % for more than 100 cycles.

Symmetrical cells with identical electrodes with  $2\text{ mAh cm}^{-2}$  of pre-deposited Li were also assembled to further evaluate the cycling stability of the modified electrodes (Fig. S3). The results further prove the higher polarization of the Cu\_LS300 that leads to lower cycling stability. In addition, the Cu\_LS1000 exhibited a more stable cycling with low overpotentials for 150 h, compared to the 110 h of the Cu sample. Thus, this preliminary analysis suggested that increasing the oxide amount beyond a certain level can reduce the overall cycling stability, further confirming that the precise control of the surface chemistry, allowed by the laser-assisted oxidation, is therefore crucial to achieve the desired electrochemical properties of the electrodes.

Cyclic Voltammetry (CV) in the 0–3 V range was performed for three cycles at a scan rate of  $0.05\text{ mV/s}$  to investigate the conversion reaction of the electrodes, as reported in Fig. 4c–d. The Cu sample exhibited low peak intensity in the first cycle and only two broad peaks, related to the decomposition of  $\text{LiNO}_3$ , the electrolyte additive, between 1 and 1.5 V, and to the SEI layer formation below 1 V. In contrast, the Cu\_LS1000 and Cu\_LS300 samples showed three distinct peaks in the cathodic scan at approximately 2 V, 1.2 V, and 0.8 V, corresponding to the multi-step conversion of  $\text{CuO}_x$  to  $\text{Li}_2\text{O}$ . Specifically, the peak at 2 V is related to the partial reduction of CuO to form a solid solution,  $\text{Cu}_{1-x}\text{Cu}^{\text{I}}\text{O}_{1-x/2}$ . This phase further reduces at 1.2 V to  $\text{Cu}_2\text{O}$ , followed by the  $\text{Li}_2\text{O}$  formation from  $\text{Cu}_2\text{O}$  occurring at 0.85 V [47–50]. Differences in peak intensities between Cu\_LS300 and Cu\_LS1000 reflect and confirm their compositional differences, as discussed in Section 3.1. For further

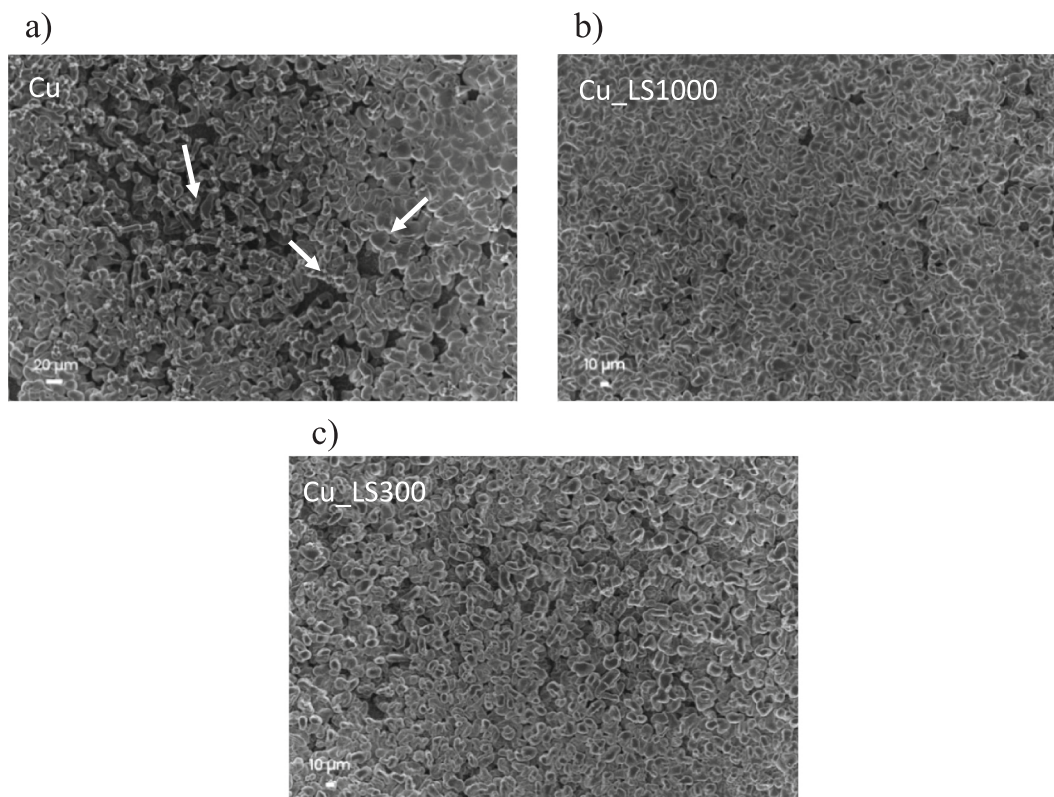


Fig. 3. SEM images of 4 mAh cm<sup>-2</sup> of metallic Li deposited on a) Cu, b) Cu\_LS1000 and c) Cu\_LS300.

clarity, Fig. S4 separates the first CV cycle for the three samples, highlighting the reaction mechanism reported above.

Above 1 V, the anodic scan shows partial re-oxidation of the SEI layer, while re-oxidation of Cu to Cu<sub>2</sub>O and CuO occurs only above 2 V vs. Li. The stability of Li<sub>2</sub>O in the defined voltage range for the Li metal anode-less battery applications was further proved by the CV profile in subsequent cycles. The CV profile obtained during the 3rd cycle is shown in Fig. 4d. The peaks related to the conversion reaction, as discussed above, are much less intense and related to the reduction of the CuO<sub>x</sub> mixture, partially regenerated during the anodic scan of the previous cycle, which further confirms that the Li<sub>2</sub>O layer formed during the first cycle was not reduced back to Li during the discharge process.

Therefore, the electrodes were tested in a full-cell configuration with LFP-based cathodes. Galvanostatic charge/discharge cycles were conducted at different C-rates of 0.1C, 0.2C, 0.5C, 1C, 2C, 3C, 4C, and 5C in order to evaluate the rate-capability behaviour of the cell. Error bars depict three experimental replicates of each cell type to confirm data reliability and reproducibility. The results are reported in Fig. 4a. It can be observed that the pure Cu sample showed a strong capacity fade during the first three forming cycles at 0.1C, from 130 mAh g<sup>-1</sup> to 119 mAh g<sup>-1</sup>. In contrast, Cu\_LS1000 showed a higher capacity of 141 mAh g<sup>-1</sup> and 137 mAh g<sup>-1</sup> for the identical cycles. The evident different behaviour suggests that the increased surface lithiophilicity donated by the laser-generated CuO<sub>x</sub>, converted to Li<sub>2</sub>O during activation, allowed for a homogeneous and compact Li layer plating and, as a consequence, less Li inventory was lost during the forming cycles. Table 3 summarizes the average specific capacities delivered by the three samples at every C-rate, calculated by averaging the 5 cycles performed at every C-rate.

At higher current densities, the Cu\_LS1000 and Cu\_LS300 samples showed superior performance across all C-rates compared to the pure Cu sample. This improvement is particularly noticeable at current densities below 3C, where the oxidized samples demonstrate reduced overpotentials that benefit the Li plating process. However, as current density increases up to 5C, the performance gap between the samples

narrows, especially in the case of Cu\_LS300.

This diminishing difference at higher current densities can be attributed to the inherently lower electrical conductivity of the oxidized Cu samples compared to pure Cu. While the reduced overpotential of the oxidized samples provided an advantage at lower C-rates by facilitating Li plating with less energy loss, at higher current densities, the increased internal resistance within the oxidized electrodes became a more significant factor, limiting their overall efficiency.

This effect is clearly illustrated by the charge-discharge curves (Fig. 5b–d), where an increase in current density results in a greater gap between the charge and discharge profiles, indicating higher polarization.

Interestingly, at a high rate of 5C, the Cu\_LS1000 sample exhibited a lower polarization of 261 mV, compared to 273 mV for the pure Cu and 290 mV for the Cu\_LS300 sample. This suggested that the Cu\_LS1000 sample managed to maintain better conductivity at high rates, likely due to the lower quantity of oxide on its surface, as previously discussed in Section 3.1.

In summary, the Cu\_LS1000 sample appeared to balance the benefits of moderate surface oxidation with minimal loss in conductivity, achieving lower polarization than Cu\_LS300 and pure Cu under high-rate conditions. This highlights the importance of carefully controlling the oxidation level during processing to optimize both the overpotential and resistance characteristics of the electrodes, tailoring them for specific operational requirements.

The Cu, Cu\_LS300 and Cu\_LS1000 were also subjected to long cycling experiments in a full cell configuration with LFP-based cathodes at a constant C-rate of 0.1C for 100 cycles. As can be noted from Fig. 6a, the capacity retention of the Cu sample is 37 % after 50 cycles and just 11 % after 100 cycles. Conversely, the Cu\_LS1000 sample exhibited 54 % and 31 % retention after 50 and 100 cycles, respectively. Interestingly, the Cu\_LS300 sample showed intermediate values, with 40 % and 15 % retention after 50 and 100 cycles.

This behaviour could be explained by the reduced Li consumption

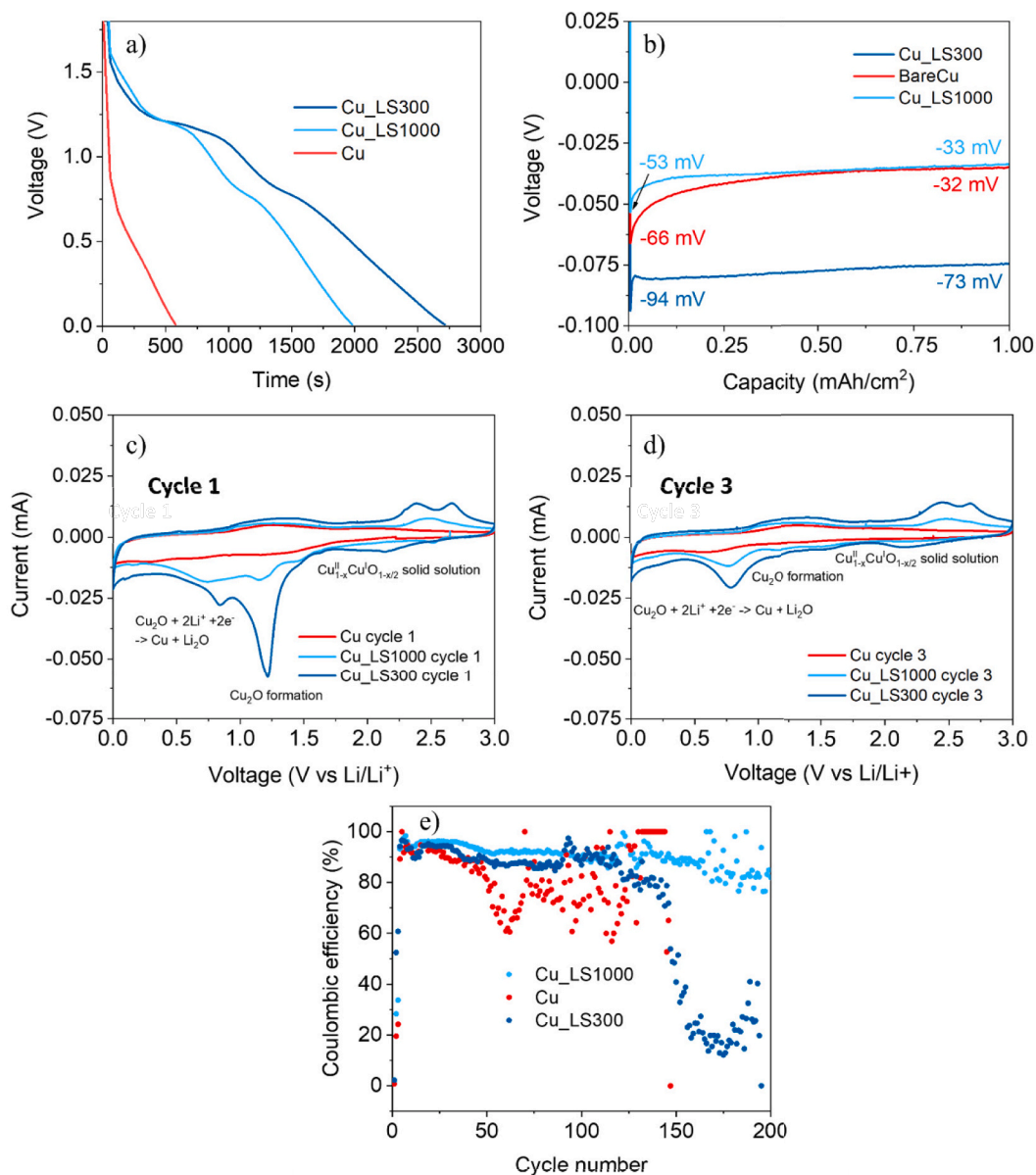


**Fig. 4.** a) Voltage profile of the conversion reaction during activation of the electrodes at 0.1 mA cm<sup>-2</sup> b) Voltage profile during the first Li plating at 0.5 mA cm<sup>-2</sup>. CV curves of a) the 1st scan and d) the 3rd scan for Cu, Cu\_LS1000 and Cu\_LS300 samples. e) CE vs cycle number for the half-cells cycled at 1 mA cm<sup>-2</sup> and 1 mAh cm<sup>-2</sup> vs Li.

**Table 3**

Values of the average specific capacity obtained at increasing C-rates from 0.1C to 5C, calculated from three repetition for each sample.

Average discharge capacity, mAh g <sup>-1</sup>			
C-rate	Cu	Cu_LS1000	Cu_LS300
0.1C	123.82	138.78	133.86
0.2C	111.00	129.39	125.53
0.5C	101.16	118.79	115.44
1C	92.32	107.51	104.71
2C	81.21	93.23	89.05
3C	70.45	81.26	74.84
4C	60.89	71.61	62.90
5C	52.21	63.23	52.71
0.1C	82.32	100.28	91.14

due to the increased lithiophilicity of the laser-processed surface, as previously discussed. On the other hand, excessive Li consumption

during the first charge caused by the CuO<sub>x</sub> to Li<sub>2</sub>O conversion reaction can have detrimental effects on the cycle life of the cell. This trend highlights the trade-off between improved interfacial lithiophilicity and irreversible lithium consumption. The more extensive surface oxidation in Cu\_LS300 results in a thicker CuO<sub>x</sub> layer, which reacts with lithium to form Li<sub>2</sub>O during the first charge. While this facilitates smoother Li plating, it also consumes a substantial portion of the available lithium inventory, which is critical in anode-less systems where Li is limited to the cathode source. The improved electrochemical performances are further confirmed by observing the Coulombic efficiency values during cycling. The average CE of the Cu sample, calculated over a window of 100 cycles, is 96.5 %. The Cu\_LS300 and Cu\_LS1000 samples showed 96.7 % and 98.2 %, respectively. Charge-discharge curves for the LFP-based full cells after 1, 10, 50 and 100 cycles are reported in Fig. 6b–d. Notably, the higher voltage hysteresis was observed during the first cycles for all three samples. This is related to the first Li plating on the substrate surface. Interestingly, Cu\_LS300 and Cu\_LS1000 showed a higher cell voltage during charge, related to the lowered Li plating

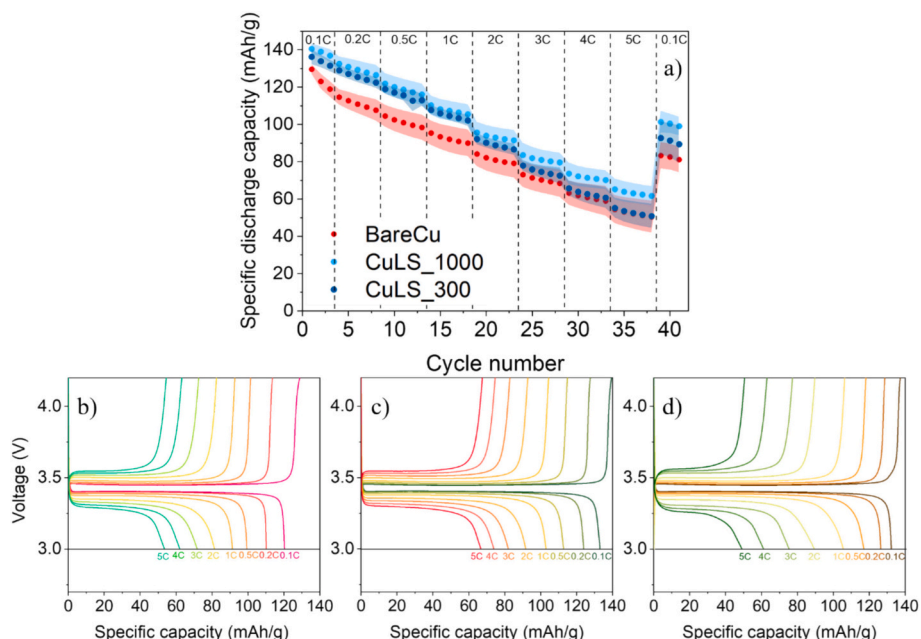


Fig. 5. a) Specific capacity vs cycle number plot of Cu, Cu\_LS1000 and Cu\_LS300 full cells vs LFP cathodes during rate capability experiments. Voltage vs Specific charge/discharge capacity for b) Cu, c) Cu\_LS1000 and d) Cu\_LS300 cells at different current densities during rate capability experiments.

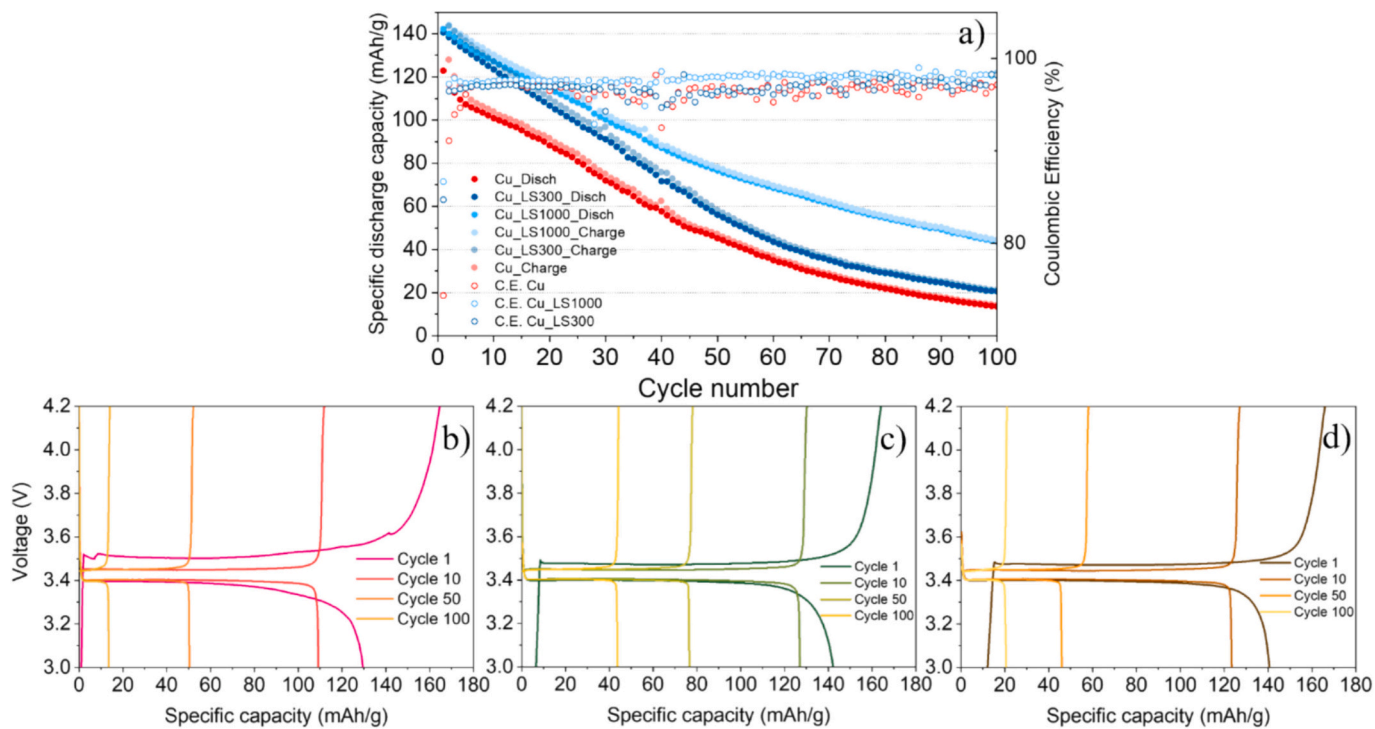


Fig. 6. a) Specific capacity vs cycle number plot of Cu, Cu\_LS1000 and Cu\_LS300 full cells vs LFP cathodes during C/10 cycling. Voltage vs Specific charge/discharge capacity for b) Cu, c) Cu\_LS1000 and d) Cu\_LS300 cells during cycling.

overpotential. The benefit is also evidenced by the CE of the first cycle, which is only 74.4 % for the Cu sample, and increases to 84.7 % for the Cu\_LS300 sample and 86.7 % for the Cu\_LS1000 sample. The CE increase is correlated to the improved reversibility of the first Li plating, which reduces the amount of Li loss as dead Li, improving the cycling stability of the cell. After the 1st cycle, the voltage hysteresis becomes similar for the three samples and remains constant during subsequent cycling. Therefore, first cycle Li plating efficiency plays a crucial role in determining the cell cycle life. In fact, the primary function of the laser-

induced oxide is to form a Li<sub>2</sub>O-rich interface upon the first activation cycle. Li<sub>2</sub>O acts as a highly lithiophilic layer due to its small lattice mismatch with metallic lithium. This layer lowers the energy barrier for lithium nucleation, facilitating uniform ionic flux and reducing the nucleation overpotential. Both Cu\_LS1000 and Cu\_LS300 benefit from this effect similarly. They exhibited nucleation overpotentials of 20 mV and 21 mV, respectively, which are significantly lower than the 34 mV observed for pristine Cu.

While Li<sub>2</sub>O favors ionic interaction, it is intrinsically an electronic

insulator with a wide bandgap of 6 eV. For lithium plating to occur, electrons must travel from the copper substrate through this SEI layer to reduce  $\text{Li}^+$  ions at the surface. As the thickness of the initial oxide layer increases, the resulting  $\text{Li}_2\text{O}$  layer becomes thicker, increasing the internal resistance and polarization of the cell.

This is quantitatively evident in the stable voltage plateau during Li plating. The Cu\_LS300 sample exhibited a much lower plateau of  $-79$  mV (indicating high resistance) compared to  $-42$  mV for Cu\_LS1000. The hindered electronic transport became critical at high current densities. In fact, at 5C, the polarization for Cu\_LS300 spiked to 290 mV, whereas the thinner, more conductive interface of Cu\_LS1000 maintained a polarization of 261 mV.

The trade-off extends beyond kinetics to the problem of lithium inventory. The conversion reactions ( $\text{Cu}_2\text{O} + 2\text{Li} \rightarrow 2\text{Cu} + \text{Li}_2\text{O}$  and  $\text{CuO} + 2\text{Li} \rightarrow \text{Cu} + \text{Li}_2\text{O}$ ) consumes active lithium from the cathode. The thicker oxide on Cu\_LS300 consumed a larger portion of the limited Li inventory during the very first cycle. Therefore, the combination of higher polarization and reduced initial Li inventory caused the rapid capacity decay seen in Cu\_LS300 (15 % retention after 100 cycles) compared to the balanced Cu\_LS1000 (31 % retention).

To better assess the contribution of surface modification to the electrochemical performances, three-electrodes cells with lithium as the reference electrode were assembled for the Cu and Cu\_LS1000 samples. The potential range was set between 3 and 4.2 V to test and separate the single contributions of the anode and the cathode over five cycles at a 0.1C rate. As can be seen in Fig. 7a–b, the cathodes present a unique voltage plateau as expected in LFP-based electrodes, as already observed in the half-cell configuration. The plating and stripping of Li at the anode take place at voltages slightly lower or higher than 0 V vs. Li, respectively. By looking at the anode voltage profiles, it is possible to note that, in the first charge, plateaus related to the  $\text{CuO}_x$  to  $\text{Li}_2\text{O}$  conversion reaction are clearly visible for the Cu\_LS1000 sample, in the range 0–1.5 V (Fig. 7c), but are not present for the Cu sample (Fig. 7d). During the first plating, the potential reached for the Li nucleation is less negative for the Cu\_LS1000 ( $-23$  mV) compared to the Cu sample ( $-54$  mV), as shown in Fig. 6e. Therefore, the anode voltage remains lower in subsequent plating, and hence, the voltage hysteresis is reduced for the cell. During discharge, plated lithium was stripped from the anode and re-oxidized to  $\text{Li}^+$  ions along with positive overpotentials. In the early stages of stripping, the potential stabilizes at around 20 mV for the Cu sample and 18 mV for the Cu\_LS1000 sample, reflecting that there is some minor difference between the electrochemical behaviour of the two samples during the initial stages of the experiment. Toward the end of the first discharge, the anode potential reaches a value of 228 mV for the Cu sample, whereas for the Cu\_LS1000 sample, it reaches a far lower value of only 66 mV.

This observation implies that the full-cell lower cut-off voltage of 3 V was achieved through an increase in the Li stripping potential, rather than complete re-intercalation of Li into the cathode. Consequently, some of the plated lithium was not efficiently inserted back into the cathode structure, leading to the formation of dead Li, unavailable for subsequent cycles. This irreversible loss of active lithium began as early as the first cycle and contributed to capacity fading over time.

The more homogeneous Li plating morphology observed for the Cu\_LS1000 sample, apparently caused a more efficient Li plating/stripping process, resulting in better reversibility. Such a difference in Li stripping behaviour between Cu and Cu\_LS1000, then, leads to a slower capacity fading rate for Cu\_LS1000, which was consistent with the trends observed in previous cycling tests. During the subsequent cycles, the stripping cut-off voltage stabilizes around 240 mV for both samples, and the differences between the two samples become less marked, therefore confirming the behaviour seen during full-cell cycling in a two-electrode setup. The voltage oscillations visible in Fig. 7a–b are related to Electrochemical Impedance Spectroscopy measurements, which were performed after every charge-discharge cycle. Fig. S5 reports the experimental Nyquist plots and the equivalent circuit used to fit the

experimental data with the Zview software, both for the Cu and the Cu\_LS1000 samples. Two semicircles are clearly visible in the plots. The high-frequency one is related to the overlapping of the anode charge transfer and the  $\text{Li}^+$  diffusion through the SEI layer [55,56], whereas the lower-frequency to the cathode charge transfer. Due to the similar time constant of the aforementioned phenomena, it is difficult to clearly separate and evaluate the specific contributions to the overall impedance. Table S3 summarizes the resistance values obtained after fitting experimental data. Interestingly, the  $R_{\text{anode}}$  values are much lower and stable for the Cu\_LS1000 sample. In contrast, the value increases upon cycling between the 1st and 5th cycles. This indicates that the  $\text{Li}_2\text{O}$ -rich interface generated during the first charge improves the kinetic properties of the electrode. This effect can be ascribed to the combination of the reduced overpotential for Li plating and the better ionic and electronic conductivity of lithium oxide, compared to SEI generated by the electrolyte decomposition [34,57,58]. Overall, these findings further confirmed the superior electrochemical performances of the laser-processed electrodes, compared to pure copper samples.

Although three-electrode measurements were primarily focused on Cu and Cu\_LS1000, the trends observed in impedance evolution (Fig. S3, Table S1) provide insight into the role of surface modification. The increasing  $R_{\text{anode}}$  values for Cu, in contrast to the stable and lower resistance observed in Cu\_LS1000, emphasize the role of a well-controlled oxide layer in enhancing interfacial kinetics. While similar measurements were not conducted for Cu\_LS300 due to its lower long-term stability and practical relevance, its performance trends already highlight the drawbacks of excessive oxidation. While  $\text{Li}_2\text{O}$  is commonly regarded as an electronic insulator due to its wide bandgap ( $\sim 6$  eV), its in situ formation during the first charge plays a critical role in stabilizing the interface in anode-less lithium metal batteries. The  $\text{Li}_2\text{O}$  layer formed through the conversion of  $\text{CuO}_x$  ( $\text{Cu}_2\text{O}$  and  $\text{CuO}$ ) during the initial activation cycle acts as an artificial solid electrolyte interphase (SEI), reducing the lithium nucleation overpotential and enabling more homogeneous and compact Li deposition. This is supported by the lower overpotentials observed during plating (Fig. 3b), the smoother morphology of plated Li (Fig. 3g–h), and the improved Coulombic efficiency and capacity retention over extended cycling (Figs. 3e and 5a). Notably, the Cu\_LS1000 sample, which exhibited moderate oxide content, achieved a favorable balance between interfacial lithiophilicity and overall conductivity, avoiding the excessive polarization observed in Cu\_LS300. These findings indicate that while excessive  $\text{Li}_2\text{O}$  can increase impedance, a controlled and limited  $\text{Li}_2\text{O}$  formation enhances the electrochemical reversibility and cycle life of the cell, thereby benefiting anode-less configurations.

Some recent studies focused on anode-less systems reported higher long-term cycling performance than the one reported here. However, it is worth noting that, direct performance comparisons must consider major differences in electrolyte formulation, formation and cycling protocols, and cell design parameters. In our case, we used a lean ether-based electrolyte (1 M LiTFSI in DOL:DME +  $\text{LiNO}_3$ ) in coin cell format without pre-lithiation, stack pressure, or hot-formation procedures. The areal loading, cut-off voltages, and N/P ratio we employ are also less optimized than in many literature examples—from dual-salt carbonate systems to ionic-liquid electrolytes—that report much longer cycle life [34,51–54]. These factors collectively favor excessive irreversible Li loss, higher impedance growth, and rapid capacity decay in anode-less cells, but, at the same time, they allow to a careful evaluation of the positive contribution of the laser-based modification of the current collector surface to the improvement of the cell electrochemical performances. Future optimization of electrolyte chemistry, formation protocols, and cell architecture may yield substantial improvement. Table S2 shows a comparison between the electrochemical performances obtained in this work and some recent literature reports obtained in similar conditions, ranging from advanced 3D-mesh collectors and alloy-skin Cu foils to simpler oxide-treated Cu. In particular, while some 3D-mesh or alloy-skin designs achieve very high Coulombic

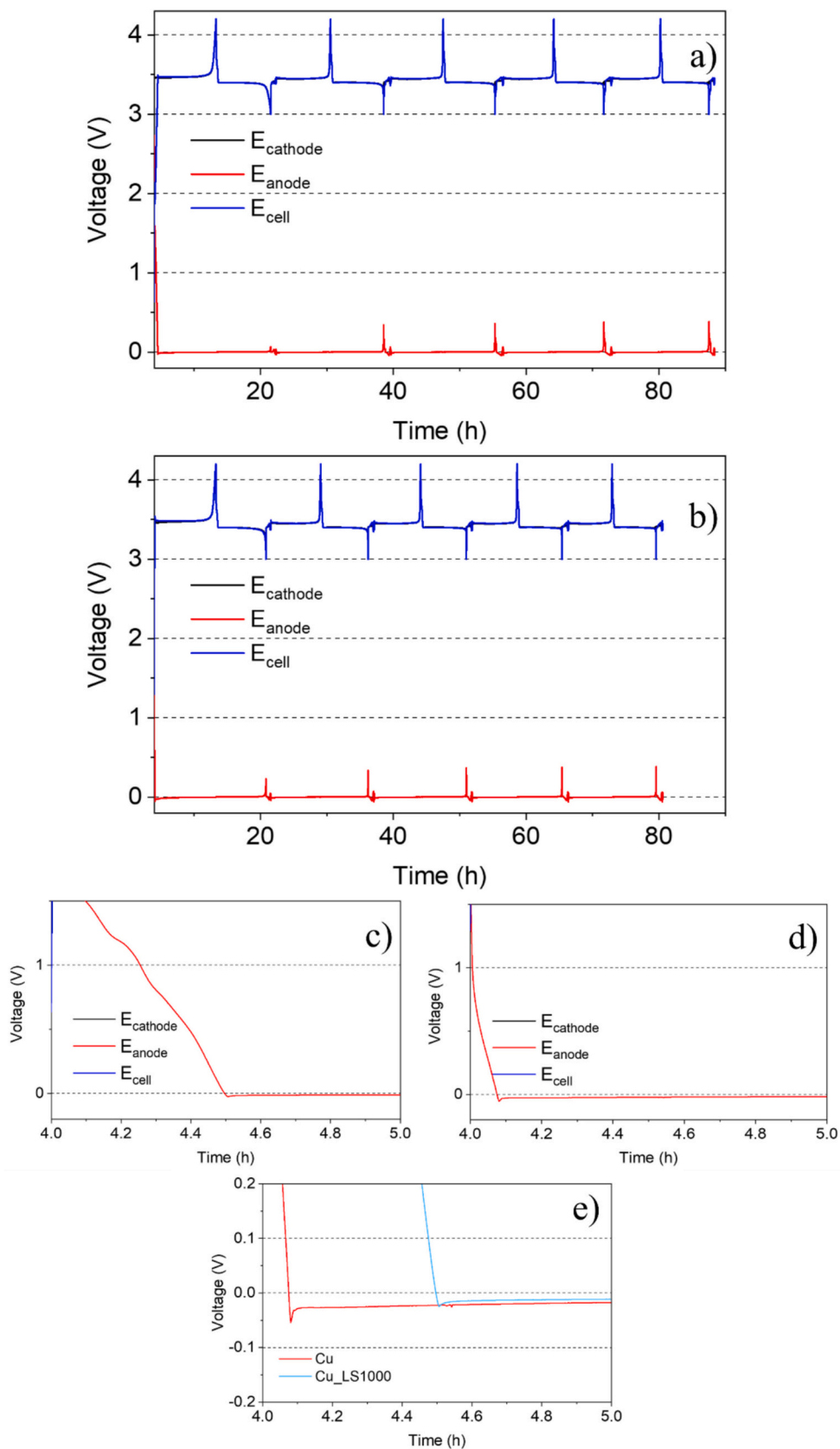


**Fig. 7.** LFP based three electrode full cell voltage profiles vs time for a) Cu and b) Cu\_LS1000. Zoom on the anodic potential during the first charge for c) Cu and d) Cu\_LS1000. e) Comparison of the anodic overpotential during Li plating between the Cu and Cu\_LS1000 cells.

efficiencies or extended cycle life, they typically rely on complex architectures or specifically optimized electrolyte formulations. In contrast, the simplicity and scalability of our laser-based oxidation is an important advantage and highlights a viable route for industrially relevant anode-less battery design. Nonetheless, the lower capacity retention after 100 cycles ( $\approx 31\%$ ) indicates there is still room for improvement compared to the best-performing examples. This suggests that combining our treated current-collector with optimized electrolyte formulations, controlled stack pressure, or 3D structural support could be viable options.

#### 4. Conclusions

Herein, a new, efficient, and cost-effective method is presented for modifying copper current collectors using laser-assisted oxidation to enhance the electrochemical performance of anode-less lithium-metal batteries (ALLMBs). The laser treatment allowed for the controlled oxidation of the copper surface with the formation of a copper oxide layer,  $\text{Cu}_2\text{O}$ , that converted to  $\text{Li}_2\text{O}$  upon the first charge. The copper oxide layer was extensively characterized and was determined to be composed of a mixture of cuprous and cupric oxide. The  $\text{Cu(II)/Cu(I)}$  ratio was dependent on careful control of the laser process parameters. The formed oxide layer promoted the uniform formation of a metallic Li layer with a reduction in Li inventory loss and, hence, improved cycling stability.

Comparing the various laser oxidation conditions under study, Cu\_LS1000 samples, moderately oxidized, exhibited the best overall performance with respect to rate capability and cycle life, offering higher CE values and cycling stability over 100 cycles. This was attributed to moderate surface oxidation, which provided a good balance between the amount of oxide and conductivity, reducing lithium plating overpotentials without increasing the cell electrical resistance. In contrast, the Cu\_LS300 samples, which had a higher degree of oxidation, showed similar initial cycling performances but then suffered from lower capacity retention due to excessive lithium consumption during the first conversion reaction.

Extensive characterizations evidenced the improved electrochemical performances of the laser-treated copper current collectors, highlighting enhanced rate capability and cycling stability in both half-cell and full-cell configurations. Therefore, these findings demonstrate that the proposed laser oxidation approach is quite promising, economical, environmentally friendly, and up-scalable for developing efficient anode-less lithium-metal batteries for industrial applications in advanced energy storage systems.

#### CRedit authorship contribution statement

**Paolo Tallone:** Writing – review & editing, Writing – original draft, Methodology, Investigation, Formal analysis, Data curation. **Silvia Spriano:** Writing – review & editing, Supervision, Resources, Funding acquisition, Conceptualization. **Daniele Versaci:** Writing – review & editing, Validation, Supervision, Methodology, Investigation, Conceptualization. **Alice Tori:** Writing – review & editing, Resources, Project administration, Funding acquisition, Conceptualization. **Silvia Bodardo:** Writing – review & editing, Resources, Project administration, Funding acquisition, Conceptualization.

#### Declaration of competing interest

The authors declare that they have no known competing financial interests or personal relationships that could have appeared to influence the work reported in this paper.

#### Acknowledgements

This publication is part of the project PNRR-NGEU which has

received funding from the MUR – DM 352/2022.

#### Appendix A. Supplementary data

Supplementary data to this article can be found online at <https://doi.org/10.1016/j.est.2026.120337>.

#### Data availability

Data will be made available on request.

#### References

- [1] B. Acebedo, M.C. Morant-Miñana, E. Gonzalo, I. Ruiz de Larramendi, A. Villaverde, J. Rikarte, L. Fallarino, Current status and future perspective on lithium metal anode production methods, *Adv. Energy Mater.* 13 (2023) 2203744, <https://doi.org/10.1002/aenm.202203744>.
- [2] G. Lu, J. Nai, D. Luan, X. Tao, X.W. (David) Lou, Surface engineering toward stable lithium metal anodes, *Sci. Adv.* 9 (2023) eadf1550, <https://doi.org/10.1126/sciadv.adf1550>.
- [3] J. Lee, S.H. Jeong, J.S. Nam, M. Sagong, J. Ahn, H. Lim, I.-D. Kim, Toward thin and stable anodes for practical lithium metal batteries: a review, strategies, and perspectives, *EcoMat* 5 (2023) e12416, <https://doi.org/10.1002/em2.12416>.
- [4] S.H. Park, D. Jun, G.H. Lee, S.G. Lee, Y.J. Lee, Toward high-performance anodeless batteries based on controlled lithium metal deposition: a review, *J. Mater. Chem. A* 9 (2021) 14656–14681, <https://doi.org/10.1039/D1TA02657G>.
- [5] S. Liu, K. Jiao, J. Yan, Prospective strategies for extending long-term cycling performance of anode-free lithium metal batteries, *Energy Storage Mater.* 54 (2023) 689–712, <https://doi.org/10.1016/j.ensm.2022.11.021>.
- [6] S. Menkin, C.A. O'Keefe, A.B. Gunnarsdóttir, S. Dey, F.M. Pesci, Z. Shen, A. Aguadero, C.P. Grey, Toward an understanding of SEI formation and lithium plating on copper in anode-free batteries, *J. Phys. Chem. C* 125 (2021) 16719–16732, <https://doi.org/10.1021/acs.jpcc.1c03877>.
- [7] Y. Tian, Y. An, C. Wei, H. Jiang, S. Xiong, J. Feng, Y. Qian, Recently advances and perspectives of anode-free rechargeable batteries, *Nano Energy* 78 (2020) 105344, <https://doi.org/10.1016/j.nanoen.2020.105344>.
- [8] K.B. Hatzell, Anode-less or anode-free? *ACS Energy Lett.* 8 (2023) 4775–4776, <https://doi.org/10.1021/acscenergylett.3c02163>.
- [9] D. Wang, W. Zhang, W. Zheng, X. Cui, T. Rojo, Q. Zhang, Towards high-safe lithium metal anodes: suppressing lithium dendrites via tuning surface energy, *Adv. Sci.* 4 (2017) 1600168, <https://doi.org/10.1002/adv.201600168>.
- [10] C. Fang, J. Li, M. Zhang, Y. Zhang, F. Yang, J.Z. Lee, M.-H. Lee, J. Alvarado, M. A. Schroeder, Y. Yang, B. Lu, N. Williams, M. Ceja, L. Yang, M. Cai, J. Gu, K. Xu, X. Wang, Y.S. Meng, Quantifying inactive lithium in lithium metal batteries, *Nature* 572 (2019) 511–515, <https://doi.org/10.1038/s41586-019-1481-z>.
- [11] B. Wu, C. Chen, L.H.J. Rajmakers, J. Liu, D.L. Danilov, R.-A. Eichel, P.H.L. Notten, Li-growth and SEI engineering for anode-free Li-metal rechargeable batteries: a review of current advances, *Energy Storage Mater.* 57 (2023) 508–539, <https://doi.org/10.1016/j.ensm.2023.02.036>.
- [12] Q. Yin, T. Li, H. Zhang, G. Zhong, X. Yang, X. Li, SEI/dead Li-turning capacity loss for high-performance anode-free solid-state lithium batteries, *J. Energy Chem.* 96 (2024) 145–152, <https://doi.org/10.1016/j.jechem.2024.04.033>.
- [13] N. Lee, J. Oh, J.W. Choi, Anode-less all-solid-state batteries: recent advances and future outlook, *Mater. Futures* 2 (2023) 013502, <https://doi.org/10.1088/2752-5724/acb3e8>.
- [14] P. Zhao, J. Pan, D. Zhang, Y. Tang, Z. Tai, Y. Liu, H. Gao, F. Huang, Designs of anode-free lithium-ion batteries, *Batteries* 9 (2023) 381, <https://doi.org/10.3390/batteries9070381>.
- [15] R. Behler, F. Badway, G.G. Amatucci, Novel electrolyte development for in situ formed Li-metal batteries using amplified solid electrolyte interphase and plating investigations, *J. Electrochem. Soc.* 171 (2024) 010501, <https://doi.org/10.1149/1945-7111/ad1552>.
- [16] S. Pal, X. Lin, P. Apostol, C. Ungureanu, D. Tie, V.R. Bakuru, D. Rambabu, N. Campagnol, A. Kachmar, C. Poleunis, G. Barozzino-Consiglio, M. Buga, A. Vlad, Ternary salt-solvent electrolytes for 5 V-class anode-less Li-metal batteries, *ACS Energy Lett.* 9 (2024) 4399–4407, <https://doi.org/10.1021/acscenergylett.4c01435>.
- [17] Q. Zhang, J. Luan, Y. Tang, X. Ji, S. Wang, H. Wang, A facile annealing strategy for achieving *in situ* controllable  $\text{Cu}_2\text{O}$  nanoparticle decorated copper foil as a current collector for stable lithium metal anodes, *J. Mater. Chem. A* 6 (2018) 18444–18448, <https://doi.org/10.1039/C8TA07612J>.
- [18] H. Kwon, J.-H. Lee, Y. Roh, J. Baek, D.J. Shin, J.K. Yoon, H.J. Ha, J.Y. Kim, H.-T. Kim, An electron-deficient carbon current collector for anode-free Li-metal batteries, *Nat. Commun.* 12 (2021) 5537, <https://doi.org/10.1038/s41467-021-25848-1>.
- [19] E. Adhitama, A.D. Refino, T. Brake, J. Pleie, C. Schmidt, F. Demelash, K. Neuhaus, S. Bornemann, S. Wiemers-Meyer, E. Peiner, M. Winter, H.S. Wasisto, T. Placke, On the direct correlation between the copper current collector surface area and 'dead Li' formation in zero-excess Li metal batteries, *J. Mater. Chem. A* 11 (2023) 7724–7734, <https://doi.org/10.1039/D3TA00097D>.
- [20] E.C. Nwaogu, Z. Bakenov, A. Nurpeissova, Three-dimensional copper current collector as an anode for rechargeable anode-less lithium-ion batteries, *Int. J.*

- Electrochem. Sci. 19 (2024) 100463, <https://doi.org/10.1016/j.joes.2024.100463>.
- [21] G.-D. Yang, Y. Liu, X. Ji, S.-M. Zhou, Z. Wang, H.-Z. Sun, Structural design of 3D current collectors for lithium metal anodes: a review, *Chem. – Eur. J.* 30 (2024) e202304152, <https://doi.org/10.1002/chem.202304152>.
- [22] R.U. Rehman Sagar, M.W. Fazal, A. Durajski, M.W. Khan, N. Mahmood, Y. Chen, Designing lithophilic interfaces for robust anode-free lithium metal batteries, *Nano Lett.* 25 (2025) 10970–10976, <https://doi.org/10.1021/acs.nanolett.5c02545>.
- [23] J. Tao, C. Zhang, X. Li, X. Chen, C. Ji, W. Wan, C. Wang, Advancing anode-less lithium metal batteries: ZnF<sub>2</sub> modification and *in situ* structural regulation for enhanced performance, *J. Mater. Chem. A* 12 (2024) 18127–18136, <https://doi.org/10.1039/D4TA02431A>.
- [24] Y. Sohn, J. Oh, J. Lee, H. Kim, I. Hwang, G. Noh, T. Lee, J.Y. Kim, K.Y. Bae, T. Lee, N. Lee, W.J. Chung, J.W. Choi, Dual-seed strategy for high-performance anode-less all-solid-state batteries, *Adv. Mater.* n/a (n.d.) 2407443, doi:<https://doi.org/10.1002/adma.202407443>.
- [25] D. Kim, J.H. Won, J. Lee, J. Seo, J.S. Park, K. Kim, H.J. Park, H.M. Jeong, 2D metal-oxide nanosheets as a homogeneous Li-ion flux regulator for high-performance anodeless lithium metal batteries, *ACS Nano* 18 (2024) 23277–23288, <https://doi.org/10.1021/acsnano.4c06149>.
- [26] J. Wang, Y. Dong, L. Li, J. Jiang, L. Fan, F. Kong, Q. Wu, L. Ni, G. Diao, M. Chen, Lithiophilic bimetallic selenides in frameworks enable excellent lithium-ion conduction solid electrolyte interphase for high-performance lithium metal batteries, *J. Power Sources* 573 (2023) 233115, <https://doi.org/10.1016/j.jpowsour.2023.233115>.
- [27] D. Lee, S. Sun, J. Kwon, H. Park, M. Jang, E. Park, B. Son, Y. Jung, T. Song, U. Paik, Copper nitride nanowires printed Li with stable cycling for Li metal batteries in carbonate electrolytes, *Adv. Mater.* 32 (2020) 1905573, <https://doi.org/10.1002/adma.201905573>.
- [28] T.-H. Hsueh, M.-C. Wang, S.-E. Liu, B.-H. Wu, Y.-C. Li, D.-G. Tsai, S.-M. Chang, A. Shiuie, K.-Y. Chin, Sputtered silver on the current collector for anode-less NMC111 gel polymer electrolyte lithium batteries, *Electrochem. Commun.* 150 (2023) 107478, <https://doi.org/10.1016/j.elecom.2023.107478>.
- [29] S. Li, L. Sun, H. Gao, Y. Long, S. Guo, Q. Jia, Y. Jiang, Z. Ye, Direct epitaxial growth of MOF arrays on Cu foils to regulate Li deposition toward lean-lithium metal batteries, *Chem. Eng. J.* 512 (2025) 162370, <https://doi.org/10.1016/j.cej.2025.162370>.
- [30] Q. Zhao, L. Zhang, T. Li, X. Zheng, X. Chen, W. Huang, Q. Xiong, Y. Zhang, Lithiophilic ZnCu alloy sites on copper current collector for high-performance Li metal anode, *Electrochim. Acta* 489 (2024) 144294, <https://doi.org/10.1016/j.electacta.2024.144294>.
- [32] W. Hu, Y. Yao, X. Huang, S. Ju, Z. Chen, M. Li, Y. Wu, CuO nanofilm-covered Cu microcone coating for a long cycle Li metal anode by *in situ* formed Li<sub>2</sub>O, *ACS Appl. Energy Mater.* 5 (2022) 3773–3782, <https://doi.org/10.1021/acsaem.2c00218>.
- [33] J. Chen, L. Dai, P. Hu, Z. Li, Facile one-step heat treatment of Cu foil for stable anode-free Li metal batteries, *Molecules* 28 (2023) 548, <https://doi.org/10.3390/molecules28020548>.
- [34] H. Xia, Y. Wang, Z. Fu, Growing cuprite nanoparticles on copper current collector toward uniform Li deposition for anode-free lithium batteries, *Appl. Surf. Sci.* 617 (2023) 156529, <https://doi.org/10.1016/j.apsusc.2023.156529>.
- [35] X. Qiu, M. Yu, G. Fan, J. Liu, Y. Wang, K. Zhao, J. Ding, F. Cheng, Growing nanostructured CuO on copper foil via chemical etching to upgrade metallic lithium anode, *ACS Appl. Mater. Interfaces* 13 (2021) 6367–6374, <https://doi.org/10.1021/acsaami.0c22046>.
- [36] J. Luan, Q. Zhang, H. Yuan, D. Sun, Z. Peng, Y. Tang, X. Ji, H. Wang, Plasma-strengthened lithiophilicity of copper oxide nanosheet-decorated Cu foil for stable lithium metal anode, *Adv. Sci.* 6 (2019) 1901433, <https://doi.org/10.1002/advs.201901433>.
- [37] A.S. Zhakypov, R.R. Nemkayeva, Y. Yerlanuly, M.A. Tulegenova, B.Y. Kurbanov, M.B. Aitzhanov, A.A. Markhabayeva, M.T. Gabdullin, Synthesis and *in situ* oxidation of copper micro- and nanoparticles by arc discharge plasma in liquid, *Sci. Rep.* 13 (2023) 15714, <https://doi.org/10.1038/s41598-023-41631-2>.
- [38] J.-Y. So, C.-H. Lee, J.-E. Kim, H.-J. Kim, J. Jun, W.-G. Bae, Hierarchically nanostructured CuO–Cu current collector fabricated by hybrid methods for developed Li-ion batteries, *Materials* 11 (2018) 1018, <https://doi.org/10.3390/ma11061018>.
- [39] S. Sedaghat, S. Nejati, L.H. Bermejo, Z. He, A.M. Alcaraz, A. Roth, Z. Li, V.G. Pol, H. Wang, R. Rahimi, Laser-induced atmospheric Cu<sub>x</sub>O formation on copper surface with enhanced electrochemical performance for non-enzymatic glucose sensing, *J. Mater. Chem. C* 9 (2021) 14997–15010, <https://doi.org/10.1039/D1TC01289D>.
- [40] M. Muszytyfaga-Staszuk, D. Janicki, K. Gawlińska-Nęceć, R. Socha, G. Putynkowski, P. Panek, Copper oxides on a Cu sheet substrate made by laser technique, *Materials* 13 (2020) 3794, <https://doi.org/10.3390/ma13173794>.
- [41] Q. Li, X. Mei, X. Sun, Y. Han, B. Liu, Z. Wang, A. Ndahimana, J. Cui, W. Wang, High-rate and excellent-cycle performance Li<sub>4</sub>Ti<sub>5</sub>O<sub>12</sub> electrodes with 3D porous copper foils as current collectors fabricated using a femtosecond laser processing strategy, *J. Energy Storage* 62 (2023) 106915, <https://doi.org/10.1016/j.est.2023.106915>.
- [42] P. Tallone, S. Spriano, D. Versaci, S. Ferraris, A. Tori, S. Bodoardo, Picosecond laser texturing of Al current collector to improve cycling performances and simplify recycling of lithium-ion batteries, *Surf. Interfaces* 51 (2024) 104659, <https://doi.org/10.1016/j.surfin.2024.104659>.
- [43] M. Shaji, K.K. Markose, K.J. Saji, M.K. Jayaraj, Investigation on the improved electrical and optical properties of trivalent boron-doped Cu<sub>2</sub>O thin film and fabrication of Cu<sub>2</sub>O:B/c-Si heterojunction diode, *J. Mater. Sci. Mater. Electron.* 31 (2020) 10724–10730, <https://doi.org/10.1007/s10854-020-03622-1>.
- [44] H. Zhang, D. Zhang, L. Guo, R. Zhang, P. Yin, R. Wang, One-pot assembly of Cu<sub>2</sub>O chain-like hollow structures, *J. Nanosci. Nanotechnol.* 8 (2008) 6332–6337, <https://doi.org/10.1166/jnn.2008.18389>.
- [45] B. Djamila, L.S. Eddine, B. Abderrhmane, A. Nassiba, A. Barhoum, *In vitro* antioxidant activities of copper mixed oxide (CuO/Cu<sub>2</sub>O) nanoparticles produced from the leaves of Phoenix dactylifera L, *Biomass Conv. Biorefr.* 14 (2024) 6567–6580, <https://doi.org/10.1007/s13399-022-02743-3>.
- [46] C. Zhang, W. Lv, G. Zhou, Z. Huang, Y. Zhang, R. Lyu, H. Wu, Q. Yun, F. Kang, Q. Yang, Vertically aligned lithiophilic CuO nanosheets on a Cu collector to stabilize lithium deposition for lithium metal batteries, *Adv. Energy Mater.* 8 (2018) 1703404, <https://doi.org/10.1002/aenm.201703404>.
- [47] M.-C. Kim, S.-J. Kim, S.-B. Han, D.-H. Kwak, E.-T. Hwang, D.-M. Kim, G.-H. Lee, H.-S. Choe, K.-W. Park, Cubic and octahedral Cu<sub>2</sub>O nanostructures as anodes for lithium-ion batteries, *J. Mater. Chem. A* 3 (2015) 23003–23010, <https://doi.org/10.1039/C5TA05455A>.
- [48] C.Q. Zhang, J.P. Tu, X.H. Huang, Y.F. Yuan, X.T. Chen, F. Mao, Preparation and electrochemical performances of cubic shape Cu<sub>2</sub>O as anode material for lithium ion batteries, *J. Alloys Compd.* 441 (2007) 52–56, <https://doi.org/10.1016/j.jallcom.2006.09.106>.
- [49] P. Wang, X.-X. Gou, S. Xin, F.-F. Cao, Facile synthesis of CuO nanochains as high-rate anode materials for lithium-ion batteries, *New J. Chem.* 43 (2019) 6535–6539, <https://doi.org/10.1039/C9NJ01015G>.
- [50] X. Chen, N. Zhang, K. Sun, Facile fabrication of CuO 1D pine-needle-like arrays for super-rate lithium storage, *J. Mater. Chem.* 22 (2012) 15080, <https://doi.org/10.1039/c2jm32183a>.
- [51] A.J. Louli, M. Coon, M. Genovese, J. deGooyer, A. Eldesoky, J.R. Dahn, Optimizing cycling conditions for anode-free lithium metal cells, *J. Electrochem. Soc.* 168 (2021) 020515, <https://doi.org/10.1149/1945-7111/abe089>.
- [52] R.V. Salvatierra, W. Chen, J.M. Tour, What can be expected from “anode-free” lithium metal batteries? *Adv. Energy Sustainability Res.* 2 (2021) 2000110, <https://doi.org/10.1002/aesr.202000110>.
- [53] R. Weber, M. Genovese, A.J. Louli, S. Hames, C. Martin, I.G. Hill, J.R. Dahn, Long cycle life and dendrite-free lithium morphology in anode-free lithium pouch cells enabled by a dual-salt liquid electrolyte, *Nat. Energy* 4 (2019) 683–689, <https://doi.org/10.1038/s41560-019-0428-9>.
- [54] J. Wang, Y. Zhou, Y. Zhuo, K. Fang, S. Wang, B. Zhao, J. Zhou, H. Wang, The challenges and strategies towards high-performance anode-free post-lithium metal batteries, *Chem. Sci.* 16 (2025) 552–574, <https://doi.org/10.1039/D4SC06630H>.
- [55] B. Wu, C. Chen, D.L. Danilov, Z. Chen, M. Jiang, R. Eichel, P.H.L. Notten, Dual additives for stabilizing Li deposition and SEI formation in anode-free Li-metal batteries, *Energy Environ. Mater.* 7 (2024) e12642, <https://doi.org/10.1002/eem2.12642>.
- [56] S. Kim, P.N. Didwal, J. Fiates, J.A. Dawson, R.S. Weatherup, M. De Volder, Effect of the formation rate on the stability of anode-free lithium metal batteries, *ACS Energy Lett.* 9 (2024) 4753–4760, <https://doi.org/10.1021/acsenerylett.4c02258>.
- [57] J. Tan, J. Matz, P. Dong, J. Shen, M. Ye, A growing appreciation for the role of LiF in the solid electrolyte interphase, *Adv. Energy Mater.* 11 (2021) 2100046, <https://doi.org/10.1002/aenm.202100046>.
- [58] R. Guo, B.M. Gallant, Li<sub>2</sub>O solid electrolyte interphase: probing transport properties at the chemical potential of lithium, *Chem. Mater.* 32 (2020) 5525–5533, <https://doi.org/10.1021/acs.chemmater.0c00333>.